Controlled Synthesis of Transition Metal Phosphide Nanoparticles to Establish Composition-Dependent Trends in Electrocatalytic Activity

Courtney A. Downes,[§] Kurt M. Van Allsburg,[§] Sean A. Tacey, Kinga A. Unocic, Frederick G. Baddour, Daniel A. Ruddy, Nicole J. LiBretto, Max M. O'Connor, Carrie A. Farberow, Joshua A. Schaidle,* and Susan E. Habas*

ACCESS | Metrics & More | Article Recommendations | SI Supporting Information

ABSTRACT: Transition-metal phosphides (TMPs) are versatile materials with tunable electronic and structural properties that have led to exceptional catalytic performances for important energy applications. Identifying predictive relationships between the catalytic performance and key features such as the composition, morphology, and crystalline structure hinges on the ability to independently tune these variables within a TMP system. Here, we have developed a versatile, low-temperature solution synthesis route to alloyed nickel phosphide ($Ni_{1.6}M_{0.4}P$, where M = Co, Cu, Mo, Pd, Rh, or Ru) nanoparticles (NPs) that retains the structure of the parent Ni_2P NPs, allowing investigation of compositional effects on activity without convoluting factors from differences in morphology and crystalline phase. As a measure of the controlled changes introduced within the isostructural series by the second metal, the binary and alloyed ternary TMP NPs supported on carbon at a nominal 5% weight loading were studied as electrocatalysts for the hydrogen evolution reaction (HER). The resultant activity of the electrocatalyst series spanned a 125 mV range in overpotential, and composition-dependent trends were investigated using density functional theory calculations on flat (0001) and corrugated ($10\bar{1}0$) $Ni_{1.67}M_{0.33}P$ surfaces. Applying the adsorption free energy of atomic H (G_H) as a descriptor for HER activity revealed a facet-dependent volcano-shaped correlation between the overpotential and G_H, with the activity trend well represented by the corrugated ($10\bar{1}0$) surfaces on which metal−metal bridge sites are available for H adsorption but not the flat (0001) surfaces. The versatility of the rational synthetic methodology allows for the preparation of a wide range of compositionally diverse TMP NPs, enabling the investigation of critical composition−performance relationships for energy applications.
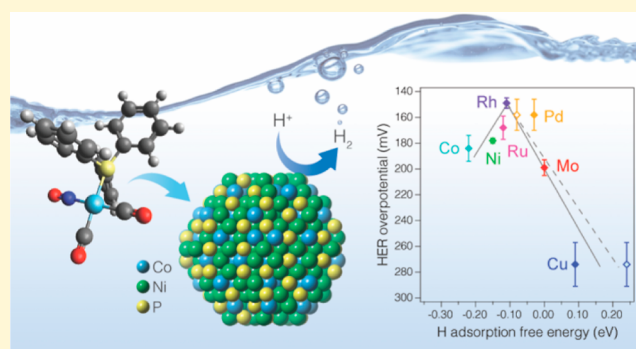
INTRODUCTION

Identifying predictive relationships between the performance of catalytic materials and key features that impact catalysis, such as the morphology, composition, and associated crystalline structure, hinges on the ability to independently control these variables within a material system. Transition-metal phosphides (TMPs), for example, are structurally complex materials that exhibit unique chemical, physical, and electronic properties due to the metal−phosphorus interactions in the crystal lattice.[1,2] These M−P interactions offer a route to precisely tune the properties of TMPs for diverse catalytic applications. TMPs are known to be highly active hydroprocessing catalysts[1,3] and, more recently, have generated significant interest as electrocatalysts due to their inherent electrical conductivity and stability.[4−6] Specifically, inexpensive and earth-abundant compositions have demonstrated activity for the hydrogen evolution reaction (HER) comparable to that of noble metal catalysts,[7,8] as well as the reduction of CO_2 to oxygenated single- and multi-carbon products.[9−14]

The composition and structure of TMPs have distinct effects on the electrocatalytic performance.[13,15−20] The introduction of a second metal to form ternary compositions ($M_xM_yP_z$), in particular, has led to catalytic performances that can exceed that of the binary parent phase. This enhancement in catalytic performance has been attributed to electronic and geometric effects that strongly influence the properties of the active sites. For example, Brock and co-workers found that $Co_{2−x}Rh_xP$ ($0.1 \leq x \leq 0.5$) and $Ni_{2−x}Ru_xP$ ($0.25 \leq x \leq 1$) nanoparticles (NPs) were more active than Co_2P and Ni_2P NPs, respectively, for the oxygen evolution reaction (OER), despite Rh_2P and Ru_2P displaying minimal OER activity.[21,22] The introduction of the

second metal into the Co_2P and Ni_2P structures was proposed to electronically activate the Co and Ni active sites, thus improving the OER performance. Similarly, for the HER, the highest activity in a series of $Ni_{2-x}Co_xP$ ($0 \leq x \leq 2$) NP electrocatalysts was observed for NiCoP ($x = 1$).[23] Density functional theory (DFT) calculations revealed that the NiCoP composition had an optimal adsorption free energy of atomic H (G_H), a key descriptor of HER activity. Within an $Fe_{2-x}Co_xP$ series, $Fe_{0.5}Co_{0.5}P$ displayed the highest HER activity, consistent with its optimal G_H.[24−26] Whereas prior studies have demonstrated the effect of changing the relative proportion of two metals in a ternary TMP on the electrocatalytic performance, fewer reports systematically evaluate the effect of the identity of the second metal on performance. Establishing such composition−performance relationships requires synthetic approaches that control the other potential compounding factors, namely, the crystal phase and morphology.

A number of synthetic approaches have been developed to access binary and ternary TMP phases. TMP nanomaterials have traditionally been synthesized using temperature-programmed reduction techniques that rely on high-temperature (>500 °C) reduction of metal and phosphorus precursors and lead to difficulty in controlling the particle morphology, phase impurities, and excess phosphorus species.[2,8] To overcome these challenges, solution-synthesis methods,[1,27−31] including those that utilize metal−phosphine complexes with tunable decomposition temperatures,[12,32−34] have enabled the synthesis of binary TMP NPs with uniform structural features. The synthesis of ternary phases, however, is complicated by differences in reactivity between two metal precursors, which can lead to phase segregation and inhomogeneities in morphology.[2] Brock et al. have developed a solution-phase arrested precipitation technique and applied it to understand the composition dependence of $Co_{2-x}Rh_xP$ NPs for water splitting reactions.[21,35] The coreduction of Co^{2+} and Rh^{3+} ions, followed by phosphidation of the resulting intermediate product at above 300 °C, allowed for investigation of a wide range of elemental ratios within a specific composition, and similar techniques have been applied to modify the elemental ratio within other ternary NP systems.[23,36−39] Alternatively, a general method for synthesizing ternary compositions in which the elemental ratio remains fixed but the identity of the second metal is changed would provide an opportunity to directly compare the impact of the second metal without convoluting factors arising from differences in the NP morphology or phase.

Here, we have developed a rational, low-temperature solution-synthesis approach using molecular precursors to incorporate a second metal into the binary Ni_2P structure. We applied this methodology to prepare ternary $Ni_{2-x}M_xP$ NPs (M = Co, Cu, Mo, Pd, Rh, or Ru) without altering the morphology and crystal phase of the parent Ni_2P NPs. The ability to independently tune the composition without modifying other features of the ternary TMP NPs allows for determination of composition-dependent catalytic activity. To this end, $Ni_{2-x}M_xP$ NPs with targeted compositions of 20 mol % M ($Ni_{1.6}M_{0.4}P$) were dispersed on a high-surface-area carbon support at a nominal loading of 5 wt %. These catalysts were then deposited on glassy carbon electrodes and investigated as electrocatalysts for the HER using a rotating disk electrode (RDE) in a 0.5 M H_2SO_4 solution. The versatility of the rational synthetic methodology enables the preparation of a wide range of compositionally diverse TMP NPs, more broadly enabling the investigation of critical composition−performance relationships for energy applications.

■ EXPERIMENTAL SECTION

Synthesis and Characterization. *General.* Synthetic manipulations to prepare metal phosphide NPs were conducted in a N_2 atmosphere using standard Schlenk techniques or in a N_2-filled Vacuum Atmospheres glovebox, unless otherwise noted. *Caution! The metal phosphide precursors have the potential to evolve pyrophoric and/or toxic phosphorus species under reaction conditions. These reactions should only be performed by trained personnel under rigorously air-free conditions.* Oleylamine (OAm, 70% technical grade) and 1-octadecene (ODE, 90%) were purchased from Sigma-Aldrich and dried prior to use by heating to 120 and 150 °C, respectively, under vacuum for 5 h and were stored in a N_2-filled glovebox prior to use. Triphenylphosphine (PPh₃, 99%), [Cu(PPh₃)H]₆, Mo(CO)₄(PPh₃)₂, RhCl(CO)(PPh₃)₂, Pd(PPh₃)₄, and RuCl₂(CO)₂(PPh₃)₂ were purchased from Sigma-Aldrich and used as received. Ni(CO)₂(PPh₃)₂ was purchased from Strem Chemicals and used as received. Co(NO)(CO)₂(PPh₃) was synthesized according to established methods.[40] The silicon powder NIST Standard Reference Material 640f was purchased from Millipore-Sigma. The carbon support (Vulcan XC 72R) was supplied by Cabot and used as received. A commercial 29.0 wt % Pt Vulcan carbon catalyst was purchased from Tanaka Kikinzoku International K.K. (electrocatalyst TEC10V30E, lot no. 1013-6231, 2 g) and was used as received for ink preparation without any thermal reduction. A 5 wt % Nafion perfluorinated resin solution in lower alcohols and water was purchased from Sigma-Aldrich (product number 274704).

Synthesis of Metal Phosphide NPs. Ni_2P NPs were prepared based on a previously described procedure.[34] Ni(CO)₂(PPh₃)₂ (0.64 g, 1.0 mmol), PPh₃ (1.05 g, 4.00 mmol), dried OAm (6.5 mL, 20 mmol), and dried ODE (6.5 mL) were combined in a three-neck round-bottom flask fitted with a condenser and two septa and heated under N_2 with rapid stirring to 250 °C at *ca.* 10 °C/min. The mixture was held at 250 °C for 15 min to form amorphous Ni−P NPs and then heated to 300 °C at *ca.* 10 °C/min. The mixture was maintained at 300 °C for 1 h, followed by removal of the heat source and ambient cooling to room temperature. The resulting NPs were recovered in CHCl₃ (*ca.* 0.1 mL), flocculated with isopropanol (*ca.* 40 mL), and separated by centrifugation at 10 000 rpm for 5 min. The NPs were redispersed in CHCl₃ (*ca.* 0.1 mL), flocculated with isopropanol (*ca.* 40 mL), separated by centrifugation, and redispersed in CHCl₃ (*ca.* 10 mL).

$Ni_{2-x}M_xP$ NPs, where M = Co, Cu, Mo, Pd, Rh, or Ru, were prepared by first forming amorphous Ni−P NPs, as described above in the procedure for the synthesis of Ni_2P NPs, by heating the reaction mixture to 250 °C and holding for 15 min. After 15 min, the heat source was removed, and the mixture was allowed to cool to room temperature. Co(NO)(CO)₂(PPh₃) (0.10 g, 0.25 mmol), [Cu(PPh₃)H]₆ (0.08 g, 0.04 mmol), Mo(CO)₄(PPh₃)₂ (0.18 g, 0.25 mmol), RuCl₂(CO)₂(PPh₃)₂ (0.19 g, 0.25 mmol), RhCl(CO)(PPh₃)₂ (0.17 g, 0.25 mmol), or Pd(PPh₃)₄ (0.29 g, 0.25 mmol) was added under flowing N_2, and then, the reaction vessel was purged with N_2 for 2 min through a needle inserted in one of the septa. The reaction mixture was heated to 300 °C at *ca.* 10 °C/min and maintained at this temperature for 1 h before cooling. The $Ni_{2-x}M_xP$ NPs were recovered as described above for the synthesis of Ni_2P NPs.

Preparation of Metal Phosphide Electrocatalysts. The carbon-supported catalysts were prepared by adding a suspension of NPs dropwise to a rapidly stirring suspension of Vulcan XC 72R in CHCl₃ (*ca.* 40 mL) to yield catalysts with nominal loadings of 5 wt % Ni_2P and 5 wt % $Ni_{2-x}M_xP$ NPs. The mixtures were sonicated for 5 min, stirred overnight, and recovered by centrifugation at 8000 rpm for 10 min. The resulting catalysts were dried under vacuum overnight. The carbon-supported catalysts were stored in an inert atmosphere but were exposed to air for short time periods (<1 h) to prepare for heat treatment and other manipulations. To remove surface organic ligands, each catalyst was thermally reduced in a tube furnace with

flowing 5% H_2 in N_2 (500 sccm). The temperature was increased at 5 °C/min to 450 °C and held for 2 h. After cooling to room temperature, the catalysts were passivated for 2 h in flowing 1% O_2/N_2 (500 sccm).

Catalyst Characterization. Thermogravimetric analyses (TGAs) of $Co(NO)(CO)_2(PPh_3)$, $RuCl_2(CO)_2(PPh_3)_2$, and $Mo-(CO)_4(PPh_3)_2$ were performed using a TA Instruments SDT Q600 integrated TGA/DSC analyzer, and the analysis of $[Cu(PPh_3)H]_6$ was performed with a SYS Evolution TGA instrument, all with a heating rate of 10 °C/min under flowing N_2. Powder X-ray diffraction (XRD) data were collected using a Rigaku Ultima IV diffractometer with a Cu Kα source (40 kV, 44 mA). Diffraction patterns were collected in the 2θ range of 20−80° at a scan rate of 4°/min. The unsupported NPs were drop-cast onto a glass slide from a chloroform suspension. Powder samples (10−20 mg) were supported on a glass sample holder with a 0.5 mm recessed sample area and were pressed into the recess with a glass slide to obtain a uniform z-axis height. The resulting patterns were compared to powder diffraction files (PDF) from the International Centre for Diffraction Data (ICDD). A NIST Si standard was used to calibrate the XRD peak positions. The crystallite sizes were calculated from XRD peak broadening using the Scherrer equation. For transmission electron microscopy (TEM) analysis of Ni_2P, the unsupported NPs were drop-cast onto continuous carbon-coated copper grids (Ted Pella part no. 01824) from chloroform suspensions. Imaging was performed using a FEI G^2 T20 Tecnai transmission electron microscope operated at 200 kV. For scanning transmission electron microscopy (STEM) with energy-dispersive X-ray spectroscopy (EDS) analysis, unsupported $Ni_{2−x}M_xP$ NPs (where M = Co, Mo, Pd, Rh, or Ru) were drop-cast onto lacey carbon-coated copper grids (SPI Supplies part no. Z3820C) from chloroform suspensions, whereas the unsupported $Ni_{2−x}Cu_xP$ NPs were drop-cast onto lacey carbon-coated gold grids (SPI Supplies part no. Z3820G) to avoid additional X-rays from the copper grid. STEM−EDS measurements were performed on a FEI F200X Talos operating at 200 kV, equipped with an extreme field emission gun (X-FEG) electron source, a high-angle annular dark-field (HAADF) detector, and a Super-X EDS system with four silicon-drift detectors (Bruker XFlash 6 series with a detector size of 120 mm^2) with a solid angle of 0.9 steradian for chemical analysis. To avoid and/or decrease any potential electron beam damage during spectroscopic analysis while maintaining a high signal-to-noise ratio, the current of the electron beam was set to 480 pA. Part of the high-resolution STEM imaging was performed on an aberration-corrected JEOL *JEM-ARM200F* TEM/STEM operated at 200 kV with a unique cold field emission gun as well as a next-generation Cs corrector (ASCOR) that compensates for higher order aberrations. High-resolution analysis was performed with a nominal beam current of 25 pA and an associated nominal resolution of 0.07 nm. Additional high-resolution STEM imaging was performed on a JEOL 2200FS TEM/STEM instrument equipped with a CEOS GmbH (Heidelberg, Germany) corrector on the illuminating lenses. The AMAG 5C mode was used to achieve a probe with a nominal 150 pA current and an associated nominal resolution of 0.07 nm. All image analysis was conducted with Gatan Microscopy Suite software, while ImageJ software was used for particle size measurements.[41] Lattice spacings were measured from the fast Fourier transforms (FFTs) of STEM images. Size distributions were determined from a manual diameter measurement of >100 particles. The metal loadings of the reduced and passivated carbon-supported catalysts were determined by inductively coupled plasma optical emission spectroscopy (ICP-OES) performed by Galbraith Laboratories (Knoxville, TN). The metal phosphide loading was determined from the measured metal content and an assumed total metal/phosphorus stoichiometry of 2:1 (Ni_2P or $Ni_{2−x}M_xP$) since the phosphorus content, determined using ICP-OES, could include unincorporated phosphorus species (*e.g.*, surface ligands).

Electrochemical Methods. *Equipment.* Testing was performed using a Metrohm Autolab PGSTAT302N potentiostat/galvanostat equipped with a FRA32M frequency response analyzer. All measurements were performed under potentiostatic control. RDEs and a modulated speed rotator (MSR) were obtained from Pine Research.

Development of the Electrode Preparation Procedure. To accurately characterize differences in the electrocatalytic activity of the NP materials, we developed a testing procedure that minimizes variability in catalyst deposition and electrode adhesion. Although the electrochemical activity of metal phosphide NPs has been studied previously on stationary Ti foils[42] and pyrolytic graphite,[24] our procedure has several notable differences. First, we based our procedure on carbon-supported NPs. Second, we used an RDE for our HER experiments, which can reduce the measurement error and variability resulting from hydrogen bubble occlusion of the electrode surface. Finally, we optimized a catalyst ink deposition procedure that resisted delamination under RDE HER conditions. In all cases, five separate electrodes were prepared and tested to obtain an estimate of the measurement error in the observed activity.

The reduced NP/carbon materials were deposited on electrodes by formation of a catalyst ink (details below). Information on preparing such inks is extensive in the hydrogen fuel cell literature and describes factors such as the solvent,[43−50] pH,[51] catalyst concentration,[52,53] ionomer concentration,[50,52,53] sonication procedures,[54] and so forth. Notably, Jung *et al.* developed an ink preparation procedure designed for benchmarking of nanopowder electrocatalysts for the HER and OER.[55] Because the ink formation parameters also depend on the properties of a specific catalyst or catalyst support, we investigated a range of parameters to improve catalyst dispersion and film quality. Our goal was to maximize the uniformity and reproducibility of our inks so that activity differences could be quantified with minimal uncertainty. The resulting ink recipe (10 mg of carbon-supported catalyst powder, 20 μL of a 5% Nafion ionomer mixture, and 0.97 mL of isopropanol) was based primarily on previous studies involving nanoparticulate materials.[55−57] Note that our concentrations of both the catalyst powder and Nafion ionomer in the ink are lower than those commonly used in fuel cell preparation owing to our objective of quantitative catalyst activity comparison rather than practical device assembly or long-term testing. Each ink was drop-cast onto five individual glassy carbon RDEs using an electronically controlled positive displacement pipette, which we found to be essential to reliable deposition. Five sequential cyclic voltammetry (CV) scans were performed on each electrode to assess relative current stability.

Catalyst Ink Preparation. The carbon-supported catalyst was weighed in a glovebox in a 2 mL glass vial. Isopropanol and a 5 wt % Nafion solution were added to the glass vial to achieve an ink with a composition of 0.97 mL of isopropanol, 20 μL of the 5 wt % Nafion solution, and 10 mg of the supported catalyst powder. The ink was homogenized using a Qsonica Misonix S-4000 horn sonicator fitted with a 1/8 in. MicroTip attachment, ensuring that the tip reached the bottom of the vial. The sonicator was configured to its lowest amplitude setting ("1") and a 10 s continuous dose length, which delivers approximately 67 J per dose to the solution. The sonication procedure consisted of two 10 s doses, each followed by immersing the vial in ice water for 1 min to dissipate the heat generated by sonication. The vial was then allowed to warm to room temperature (*ca.* 10 min) before the drop-casting procedure.

Deposition of Catalyst Inks on RDEs. The catalyst inks were drop-cast onto five individual RDEs having 5 mm diameter glassy carbon disk working surfaces surrounded by a 15 mm outer diameter poly(tetrafluoroethylene) (PTFE) shroud (Pine Research, AFE5T050GC). The electrodes were prepared by polishing with 0.05 μm alumina and were placed with their working electrode surfaces facing up. The catalyst ink (10 μL) was dropped onto each electrode using an electronic positive-displacement autopipette (Eppendorf Repeater E3), resulting in a mass loading of supported catalyst powder of 0.51 mg/cm^2. The electronic autopipette was used because control of the dispensing speed was critical in controlling splatter and spillover from the glassy carbon onto the PTFE shroud (when the dispensing rate was too fast), as well as droplet adhesion to the pipette tip (when the dispensing rate was too slow). When needed, two successive 5 μL drops were used instead for electrodes with a propensity for spillover. The electrodes were allowed to dry with minimal movement and airflow for 2−24 h before measurement.

Electrochemical Hydrogen Evolution Testing via CV. HER measurements were performed in a 0.5 M sulfuric acid solution (prepared from deionized water and EMD Millipore Suprapur 96% sulfuric acid) in a glass H-cell with the counter electrode separated from the working and reference electrodes by a glass frit. The cell was cleaned between measurements using aqua regia and deionized water. The working side of the cell was continuously purged with bubbling hydrogen. A silver/silver chloride reference electrode and carbon rod counter electrode were used. The potential measured using the reference electrode was adjusted to be relative to the reversible hydrogen electrode potential, after measurement, by observation of the open-circuit potential of a Pt wire electrode inserted into the working electrode compartment. The glassy carbon rotating disk working electrodes were rotated at 1600 rpm for all measurements except alternating current (AC) impedance, which was observed in quiescent solution.

For each catalyst material, the cell and solution resistances were first characterized by AC impedance on the first working electrode. The working electrode position was then maintained for the remainder of the measurement. The solution resistance was determined as the lowest-magnitude real-axis intercept on a Nyquist plot of the AC impedance. No *iR* compensation was used during measurement; potentials were corrected for 100% of the estimated voltage drop due to solution resistance during data processing. After AC impedance measurement, rotation and hydrogen bubbling were resumed and linear sweep voltammetry (LSV) at −20 mV/s was used to determine the scan limits for CV. LSV was stopped after reaching 5 mA (~25 mA/cm²) of peak current. Five successive CV scans at 5 mV/s were then performed starting from the open-circuit potential (or, occasionally, from a more negative potential to shorten the measurement time) and reversing at the potential identified above as sufficient to achieve 5 mA. The five-scan CV measurement was then repeated for each of the four remaining electrodes. Voltammograms were plotted giving the cathodic potential and current a negative sign. Cathodic overpotential required to achieve a cathodic current of 10 mA/cm² is reported as an absolute value ($|\eta|$).

Post-HER Characterization of the NP Catalyst. The post-HER properties of a $Ni_{1.6}Rh_{0.4}P/C$ catalyst were studied by preparing a large sheet electrode. A catalyst ink comprising 60 mg of 3.7 wt % $Ni_{1.58}Rh_{0.42}P/C$, 120 μL of a 5 wt % Nafion solution, and 3 mL of isopropanol (approx. double the concentration used above, for more efficient deposition) was homogenized by sonication as described above. This ink was then hand-painted in its entirety, followed by an additional 1 mL of isopropanol used to rinse the ink container and brush, onto a 6 cm × 5 cm (30 cm²) area on a sheet of Spectracarb 2050A-0850 carbon paper (Fuel Cell Store). During painting, the carbon paper was held by vacuum onto a heated stage at 80 °C. An additional 2 cm at the top of the carbon paper sheet was left unpainted for electrode assembly for a total sheet size of 8 cm × 5 cm. The sheet was weighed before and after hand-painting and had increased in mass by 45.7 mg, as compared to the theoretical value of 66 mg (60 mg catalyst + 6 mg Nafion). The difference between expected and observed loadings is attributed to the catalyst and/or Nafion remaining in the brush used to paint the electrode. The observed loading of the catalyst averaged over the 30 cm² active area, assuming about 10% of the observed mass is accounted for by Nafion, is 1.37 mg/cm². The painted sheet was then cut into two 8 × 2.5 cm pieces, one for pre-HER analysis and one for post-HER analysis. The piece to be used for the electrochemical HER was prepared by affixing a coiled copper wire to the uncoated upper area using a two-part silver epoxy. The exposed copper wire and silver epoxy were then completely sealed using a combination of sealant epoxy (3M Scotch-Weld DP460NS) and a glass tube to prevent contact between the electrolyte and these parts of the electrode assembly. The resulting electrode was tested in a H-cell where the working and counter compartments (60 mL of electrolyte in each) were separated by a Nafion 115 membrane sealed with an o-ring. The HER conditioning used a 0.5 M sulfuric acid electrolyte, a 3 M Ag/AgCl reference electrode, and a Pt mesh counter electrode. After determining solution resistance by AC impedance, LSV at −20 mV/s was used to

determine scan limits for CV cycling. Five successive CV scans at 5 mV/s were then performed from the open-circuit potential to a potential sufficient to achieve *ca.* 15−20 mA/cm² of peak current. After HER conditioning, the working electrode was washed with deionized water and allowed to air dry. Identical coupons were then cut from both the pre- and post-HER electrodes for various characterization techniques, including XRD (*ca.* 4 cm²), ICP-OES (*ca.* 5 cm²), and STEM−EDS (*ca.* 2 cm²). The sample for XRD was used without preparation. The samples for ICP-OES were sent intact to be digested by the analytical lab. For STEM−EDS, the carbon-supported NPs from the electrode sample were redispersed into ethanol using a bath sonicator for 5 min and then dip-coated onto lacey carbon-coated copper grids.

■ COMPUTATIONAL METHODS

The Vienna *ab initio* simulation package was used to implement DFT calculations.[58,59] The generalized-gradient approximation (GGA) was used *via* the Perdew−Burke−Ernzerhof formalism to describe the exchange-correlation functional.[60] Projector augmented-wave potentials with valence wavefunctions expanded through a plane-wave basis set with a cutoff energy of 500 eV were used to capture interactions between electrons and ions.[61,62] Spin-polarized adjustments were made to the GGA to describe the magnetic ordering of the slabs considered in this study. Dispersion corrections to the calculated structures and energetics were included through the D3 method by Grimme *et al.*[63]

To model the ternary $Ni_{2-x}M_xP$ catalyst systems (M = Co, Cu, Mo, Ni, Pd, Rh, or Ru), two surface facets were considered, the $(10\bar{1}0)$ and the (0001) surfaces, based on a previous theoretical work indicating that these surfaces are two of the dominant exposed facets on Ni_2P NPs.[64] The (0001) surface is the Ni_2P surface most commonly used in previous computational studies.[23,24,65−67] Vacuum layers at least 10 Å thick were employed to separate each successive slab in the *z* direction. In all calculations, the bottom half of each studied $Ni_{2-x}M_xP$ surface was fixed in its respective bulk-truncated position, while the top half could freely relax. For each $(10\bar{1}0)$ and (0001) surface considered in this work, 8 × 8 × 1 and 6 × 6 × 1 Monkhorst−Pack *k*-point meshes were used to sample the surface Brillouin zone, respectively.[68] Ionic convergence occurred when the forces acting upon each atom fell below 0.02 eV/Å.

To quantify the strength of adsorption of atomic hydrogen, the binding energy (E_B) was determined by

$$E_B = E_{total} - E_{clean} - E_{gas} \tag{1}$$

where E_{total}, E_{clean}, and E_{gas} are the energy of the adsorbate + substrate complex, clean surface, and gas-phase adsorbate ($1/2 H_2$), respectively. Temperature corrections were applied to the most-stable adsorption structures for each surface to calculate G_H as follows

$$G_H = (E + ZPE - TS)_{total} - E_{clean} - (E + ZPE - TS)_{gas} \tag{2}$$

In eq 2, *E* is the total energy, *ZPE* is the zero-point energy, *T* is the absolute temperature, and *S* is the entropy. The subscripts "total", "clean", and "gas" refer to the adsorbate + surface complex, the clean surface, and the gas-phase reference ($1/2 H_2$), respectively. By this definition, more negative E_B and G_H values correspond to stronger interactions between the surface and adsorbate. The ZPE and *S* were calculated using vibrational-frequency analyses through a Hessian matrix calculated *via* a second-order finite-difference approach. In these calculations, adsorbed H was freely relaxed, all slab atoms were fixed, and bonds were oscillated using a step size of 0.015 Å.

The optimized lattice parameters for bulk Ni_2P were 5.80 and 3.35 Å for *a* and *c*, respectively, which agree well with the experimental values of 5.86 and 3.38 Å, respectively.[69] To calculate the effect of a second metal on the calculated lattice parameters, one of the six Ni atoms in the bulk primitive cell was substituted with each second metal. In the primitive cell, there are two unique metal positions for the second metal to substitute into the Ni_I and Ni_{II} positions (see Figure S2).[64] The preferred position for M substitution and the effect

of each second metal on the DFT-calculated lattice parameters is summarized in Table S2.

In both the $(10\bar{1}0)$ and the (0001) ternary $Ni_{2-x}M_xP$ model surfaces, there are 12 metal-atom positions. Two Ni atoms in each ternary metal−phosphide system were substituted with each M to achieve a ternary metal−phosphide composition of $Ni_{1.67}M_{0.33}P$, that is, to achieve an x value of 0.33. This x value of 0.33 is close to the target experimental value of 0.40 and within the experimental range of 0.31−0.46 (see Results and Discussion). To determine the optimal metal positions for each second metal atom (M), the positions were optimized for one M atom in the freely relaxed top half of the slab and another M atom in the fixed bottom half of the slab. $Ni_{1.33}M_{0.67}P$ systems (M = Cu and Pd) with a 50:50 ratio of Ni/Cu and Ni/Pd in the freely relaxed surface layers (*i.e.*, M-enriched surfaces) were also considered based on the respective EDS elemental maps discussed in the Results and Discussion section.

For the (0001) surface, there are two bulk terminations, the Ni_3P_2- and the Ni_3P-terminated surfaces. Based on the DFT calculations presented here for the pristine $Ni_2P(0001)$ surface and for each ternary $Ni_{1.67}M_{0.33}P(0001)$ slab, the stoichiometric Ni_3P-surface termination is most stable (see Table S4), consistent with prior computational studies of Ni_2P surface stability at a low P chemical potential (μ_P).[64,70] At high μ_P, consistent with Ni_2P synthesis conditions, the P-enriched P−$Ni_3P_2(0001)$ surface termination is predicted to be most stable (*i.e.*, Ni_3P_2 termination with an adsorbed P adatom). Both the Ni_3P- and P-Ni_3P_2-terminated $Ni_{1.67}M_{0.33}P$-(0001) surfaces were modeled as possible representative catalyst surface models. The $(10\bar{1}0)$ surface is composed of two different Ni_2P planes, denoted as A and B (they differ in the positions of the two distinct phosphorus atoms in the bulk unit cell, P_I and P_{II}), stacked with an −ABB− repetition. Thus, there are three possible $(10\bar{1}0)$ surface terminations, denoted ABB−, BAB−, and BBA−. He and co-workers showed that the stoichiometric ABB-terminated and P-enriched P-BAB-terminated $(10\bar{1}0)$ surfaces are most stable at low and high μ_P, respectively;[64] thus, these two surfaces are considered in this analysis.

■ RESULTS AND DISCUSSION

The Ni_2P NPs were prepared *via* the thermal decomposition of $Ni(CO)_2(PPh_3)_2$ in OAm and ODE with PPh_3, similar to the reported procedure.[34] The $Ni_{2-x}M_xP$ (M = Co, Cu, Mo, Pd, Rh, or Ru) NPs were synthesized using a two-step synthesis route. Amorphous Ni−P NPs, which were previously characterized by our group and others as an intermediate to crystalline Ni_2P,[34,71−73] were targeted here as precursors to facilitate the incorporation of a second metal and formation of $Ni_{2-x}M_xP$ NPs.[37] The amorphous Ni−P NPs were formed by the thermal decomposition of $Ni(CO)_2(PPh_3)_2$ in OAm and ODE with PPh_3 at 250 °C. Molecular precursors for the second metal were identified based on the commercial availability or ease of preparation, air stability, and decomposition temperature. TGA data for $Ni(PPh_3)_2(CO)_2$, Rh-$(PPh_3)_2(CO)Cl$, and $Pd(PPh_3)_4$ in an inert atmosphere were previously reported[34] and demonstrated high-temperature decomposition events with precipitous weight losses beginning at 204, 274, and 212 °C for the Ni, Rh, and Pd complexes, respectively. The $Co(NO)(CO)_2(PPh_3)$ and $[Cu(PPh_3)H]_6$ complexes, reported here (Figure S1), exhibited a small, gradual weight loss around 120 °C and then more rapid weight loss indicative of full decomposition around 220 and 250 °C, respectively. $Mo(CO)_4(PPh_3)_2$ demonstrated precipitous weight loss beginning at 160 °C, while $RuCl_2(CO)_2(PPh_3)_2$ decomposed gradually starting at 230 °C. The resulting ceramic yields at 500 °C for the Co, Cu, and Mo complexes were greater than those expected for the common metal products and could contain O and/or P. The Ru complex had

a significantly higher ceramic yield of 45 wt % that could indicate incomplete decomposition under these conditions.

After the room-temperature addition of the molecular precursor of the second metal, the reaction mixture was heated to 300 °C to promote precursor decomposition, alloying, and crystallization of the ternary TMP NPs. The $Ni_{2-x}M_xP$ NPs retained the hexagonal structure of Ni_2P, and all observed powder XRD peaks were attributed to Ni_2P (Figure 1). Elemental analysis of the metal composition, determined by ICP-OES, revealed $Ni_{2-x}M_xP$ compositions ranging from $x = 0.31$ to $x = 0.46$ (Table 1).
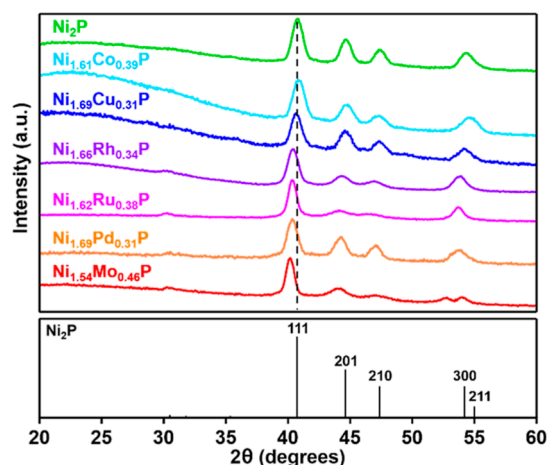

Figure 1. XRD patterns of Ni_2P and $Ni_{2-x}M_xP$ NPs with the corresponding Ni_2P reference pattern (PDF 01-089-2742), below.

Table 1. Compositions Determined by ICP-OES and Particle Sizes Determined by XRD and STEM for Ni_2P and $Ni_{2-x}M_xP$ NPs

composition	XRD size (nm)	STEM size (nm)
Ni_2P	9.8	10.0 ± 0.9
$Ni_{1.61}Co_{0.39}P$	10.0	9.8 ± 1.0
$Ni_{1.69}Cu_{0.31}P$	8.6	9.5 ± 3.8
$Ni_{1.66}Rh_{0.34}P$	9.7	9.5 ± 0.8
$Ni_{1.62}Ru_{0.38}P$	9.5	11.8 ± 1.2
$Ni_{1.69}Pd_{0.31}P$	9.2	9.2 ± 1.1
$Ni_{1.54}Mo_{0.46}P$	10.4	11.6 ± 1.1

Upon introduction of *ca.* 20 mol % M into the Ni_2P structure, the reflections in the XRD patterns shifted, as has previously been observed for $Ni_{2-x}M_xP$ NPs.[22,38] For all metals except Co, patterns shifted to lower 2θ values, indicative of lattice expansion due to substitution of the smaller-atomic-radius Ni with the larger-atomic-radius metal. The magnitude of this shift was dependent on the atomic radius of the second metal with the largest shift observed for $Ni_{1.54}Mo_{0.46}P$ (Table S1). Evaluation of the preferred Ni-substitution site and optimized lattice constants in bulk $Ni_{1.67}M_{0.33}P$ (Figure S2, Table S2) by DFT calculations supported the observed shifts in the XRD peak positions (Table S1). Additionally, for M = Rh, Ru, and Mo, the (201) and (210) reflections broadened relative to the (111) and $(300)/(211)$ reflections. This suggests that modifications of the local Ni_2P structure occurred with the addition of the larger second metal, while the overall hexagonal crystal structure was retained.[21,22]

The Ni_2P NPs are solid particles exhibiting a spherical morphology with an average size of 10.0 ± 0.9 nm, as
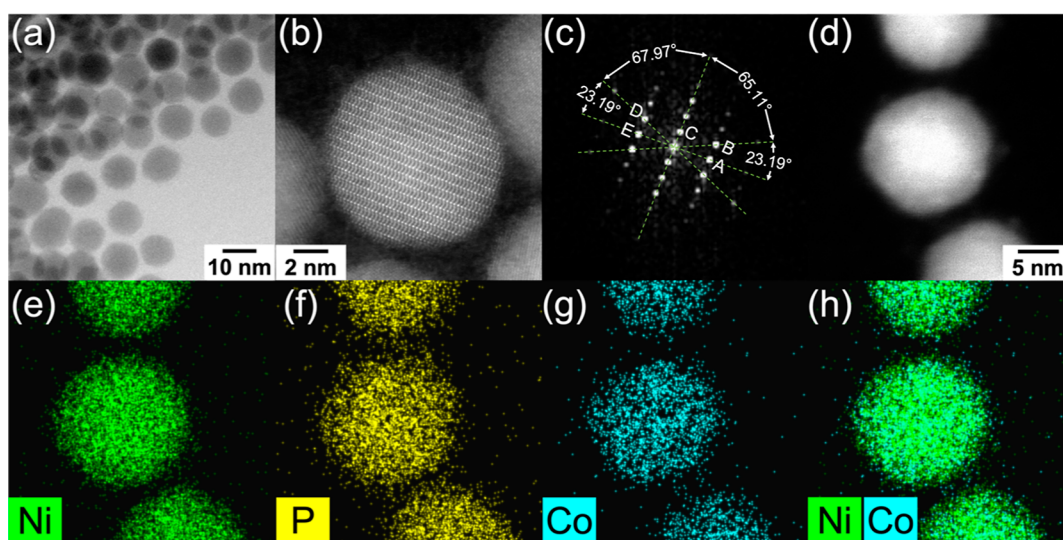
Figure 2. (a) BF-STEM image of $Ni_{1.61}Co_{0.39}P$ NPs; (b) high-resolution HAADF-STEM image with the (c) FFT oriented along the $[11\bar{2}2]$ direction; and (d) HAADF-STEM image for EDS analysis and associated EDS elemental maps for (e) Ni, (f) P, (g) Co, and (h) Ni and Co overlaid.
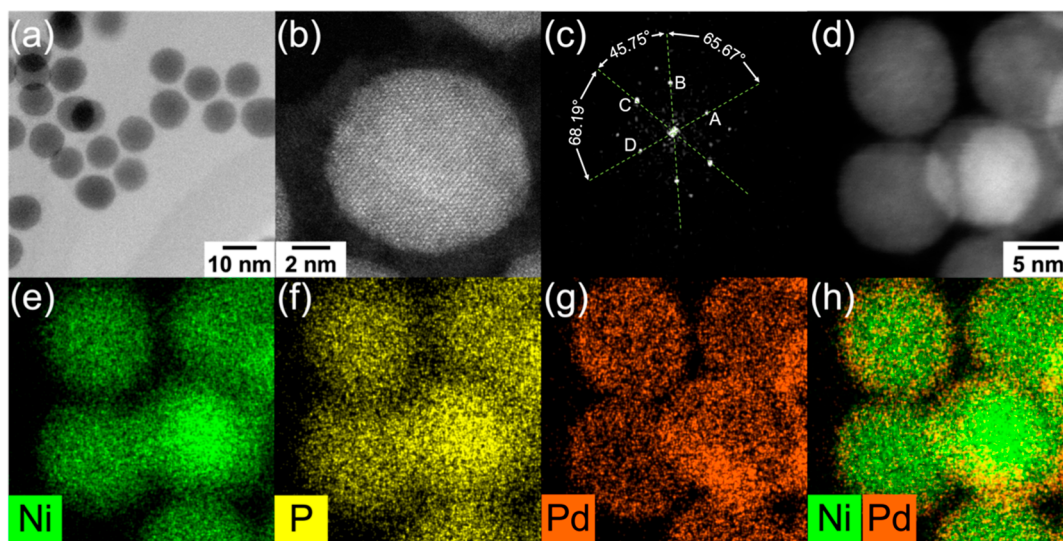

Figure 3. (a) BF-STEM image of $Ni_{1.69}Pd_{0.31}P$ NPs; (b) high-resolution HAADF-STEM image with the (c) FFT oriented along the $[12\bar{3}3]$ direction; and (d) HAADF-STEM image for EDS analysis; and associated EDS elemental maps for (e) Ni, (f) P, (g) Pd, and (h) Ni and Pd overlaid.

determined by TEM analysis (Figure S4 and Table 1). The spherical morphology was maintained across the series of $Ni_{2-x}M_xP$ NPs, as confirmed by bright-field (BF)-STEM analysis (Figures 2a, 3a, and S4a−S7a), and the average sizes ranged from 9.2 to 11.8 nm with narrow distributions for all compositions except $Ni_{1.61}Cu_{0.39}P$ (Figure S5a). We hypothesize that the wide size distribution of $Ni_{1.61}Cu_{0.39}P$ (9.5 ± 3.8 nm) was due to the less well-controlled or incomplete decomposition of the $[Cu(PPh_3)H]_6$ precursor. A similar issue was previously observed when using this molecular precursor to synthesize Cu_3P NPs.[12] Crystallite sizes were calculated for all compositions by applying the Scherrer equation to the (111) XRD peaks, and the calculated sizes were in good agreement with the particle sizes measured by STEM (Table 1).

The high-resolution HAADF-STEM analysis of $Ni_{1.61}Co_{0.39}P$ NPs, shown in Figure 2b with the corresponding FFT (Figure

2c, Table S5) oriented along the $[11\bar{2}2]$ direction, is characterized by ordered lattice fringes confirming the crystallinity and hexagonal phase of the NPs. The structural analysis is consistent for all $Ni_{2-x}M_xP$ NPs, as shown in Figures 3a−c and S4c−S7c and described in Tables S6−S10. The EDS elemental mapping of $Ni_{2-x}M_xP$ showed relatively uniform distributions of Ni, P, and M (when M = Co, Rh, Ru, or Mo) within the NPs (Figures 2e−h and S5−S7). For $Ni_{1.61}Cu_{0.39}P$ and $Ni_{1.69}Pd_{0.31}P$ NPs, EDS revealed that the distributions of Cu and Pd were more concentrated at the NP surfaces (Figures S5e−h and 3e−h). In the case of $Ni_{1.61}Cu_{0.39}P$, the less well-controlled decomposition of the $[Cu(PPh_3)H]_6$ complex, as discussed above, may play a role in the surface enrichment. For the larger-atomic-radius Pd, surface enrichment may have limited modifications of the local Ni_2P structure that led to the relative broadening of the (201) and

Table 2. Weight Loading, Overpotential Required to Reach 10 mA/cm² (η), Tafel Slope, and Exchange Current Density for Ni_2P/C, $Ni_{2-x}M_xP/C$, and Commercial Pt/C, Ordered by Increasing Overpotential

catalyst	wt % on C[a]	overpotential to achieve 10 mA/cm², η (mV)[b]	Tafel slope (mV/dec)[c]	exchange current density (mA/cm²)[c]
Pt/C	29	42 ± 25	25 ± 10	0.65 ± 0.09
$Ni_{1.66}Rh_{0.34}P/C$	4.1	149 ± 4	58.5 ± 0.4	0.029 ± 0.005
$Ni_{1.69}Pd_{0.31}P/C$	4.6	158 ± 12	96 ± 9	0.26 ± 0.05
$Ni_{1.62}Ru_{0.38}P/C$	4.8	168 ± 9	70 ± 5	0.04 ± 0.01
Ni_2P/C	5.4	178 ± 2	64.2 ± 0.4	0.016 ± 0.001
$Ni_{1.61}Co_{0.39}P/C$	4.9	184 ± 10	68 ± 4	0.019 ± 0.002
$Ni_{1.54}Mo_{0.46}P/C$	5.1	199 ± 6	65 ± 3	0.008 ± 0.002
$Ni_{1.69}Cu_{0.31}P/C$	5.9	274 ± 17	101 ± 8	0.020 ± 0.003

[a]Weight loading of the metal or metal phosphide on carbon as determined by ICP-OES. [b]Five electrodes were tested for each catalyst. For each electrode, the potentials at 10 mA/cm² of the forward and reverse sweeps of the third consecutive CV scan were averaged (see Figure S19). The resulting five potentials were averaged to determine the overall average and standard deviation. [c]From a fit to the linear region; values and standard deviations determined by averaging the values for all five electrodes (see Figure S20). Exemplary fits are shown in Figure 4b.

(210) reflections observed in the XRD patterns of M = Rh, Ru, and Mo.

Electrochemical activity measurements were performed using $Ni_{2-x}M_xP$ NPs supported on carbon (Vulcan XC 72R). The NPs were supported with a targeted weight loading of 5% and thermally reduced at 450 °C in 5% H_2 before passivation with 1% O_2. Electrochemical analysis of colloidal NPs has indicated that the presence of surface ligands reduces the electrochemically active surface area (ECSA), thus inhibiting the catalytic activity.[30,74] Reduction at 450 °C in H_2 has been established as a method to remove organic surface ligands from metal phosphide NPs.[7,12,75] Elemental analysis of the reduced and passivated $Ni_{2-x}M_xP/C$ revealed weight loadings ranging from 4.1 to 5.9% (Table 2). XRD patterns of the NPs after supporting and thermal reduction confirmed retention of the Ni_2P hexagonal structure, with no appreciable alterations (Figures S9−S15). Previous TEM analysis indicated no appreciable changes to the particle size of Ni_2P NPs following the supporting procedure and thermal reduction.[75]

Electrodes were prepared for each catalyst by drop-casting an ink consisting of $Ni_{2-x}M_xP/C$ or Ni_2P/C, Nafion, and isopropanol onto a glassy carbon RDE, as seen in literature methods for NP- and carbon-supported materials (see the Experimental Section).[7,42,55,76,77] A commercial 29 wt % Pt/C material was also included as a reference. This material did not suspend as well using the ink preparation method optimized for the NP catalysts, which may have caused the greater variability observed for Pt (vide infra). Figure 4a shows the voltammograms for $Ni_{2-x}M_xP/C$, Ni_2P/C, and Pt/C. Stable current responses were observed for five consecutive CV scans across the series of NP catalysts (Figure S18). To reduce contributions from surface contaminants and allow for catalyst equilibration,[78] the third scan is presented in Figure 4a.

Modulation of the HER activity of Ni_2P by controlled doping was quantified by measuring the overpotential required to achieve a cathodic current of 10 mA/cm² (η; Table 2). The parent Ni_2P NPs exhibited an η of 178 ± 2 mV, activity that is consistent with that previously reported for Ni_2P NPs.[7] Markedly different HER activities were observed across the $Ni_{2-x}M_xP$ NP series, with η ranging from 149 mV for the most active catalyst, $Ni_{1.66}Rh_{0.34}P$, to 274 mV for the least active, $Ni_{1.61}Cu_{0.39}P$ (Table 2). Because determination of the ECSA via the double-layer capacitance is challenging for carbon-supported materials, catalyst comparisons were performed using a geometric surface area basis. This approach relies on our observations that the particles maintain their size and
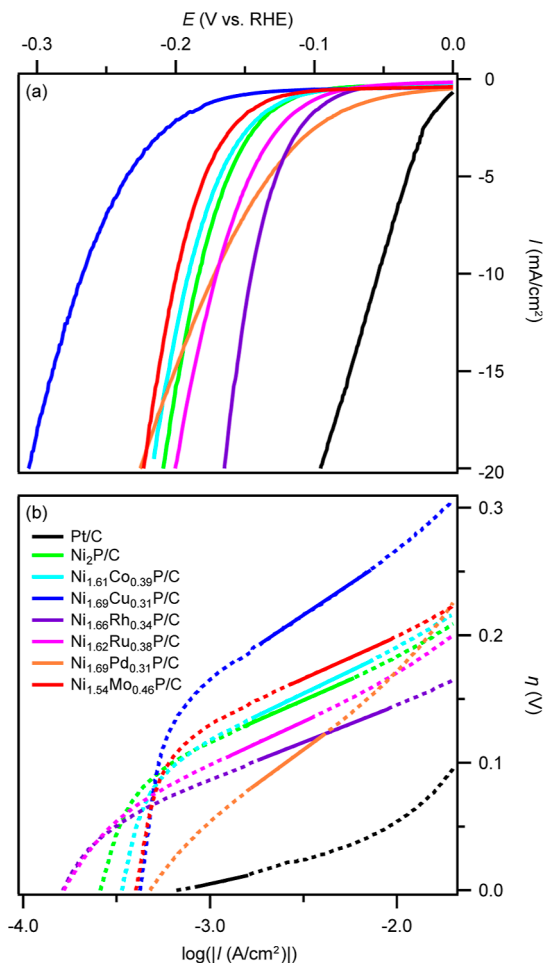

Figure 4. (a) Voltammograms (cathodic sweep only, 5 mV/s) and (b) Tafel plots for $Ni_{2-x}M_xP/C$ (nominally 5 wt %; see Table 2) and Pt/C (29 wt %) catalysts in H_2-saturated 0.5 M H_2SO_4 at room temperature, with both experimental data (dashed) and linear fits (solid; Table 2) shown (catalyst loading = 0.51 mg/cm²; NP loading ≈ 0.025 mg/cm²). The legend for both plots is shown in (b).

shape and are well dispersed, upon carbon immobilization, allowing an assumption of a similar ECSA across the series.[75] We also compared the catalysts normalized on per-milligram NP and per-mole metal bases in Figure S16, which revealed no significant changes in activity ranking except that the gap in activity between Pt and the $Ni_{2-x}M_xP$ NPs was much smaller
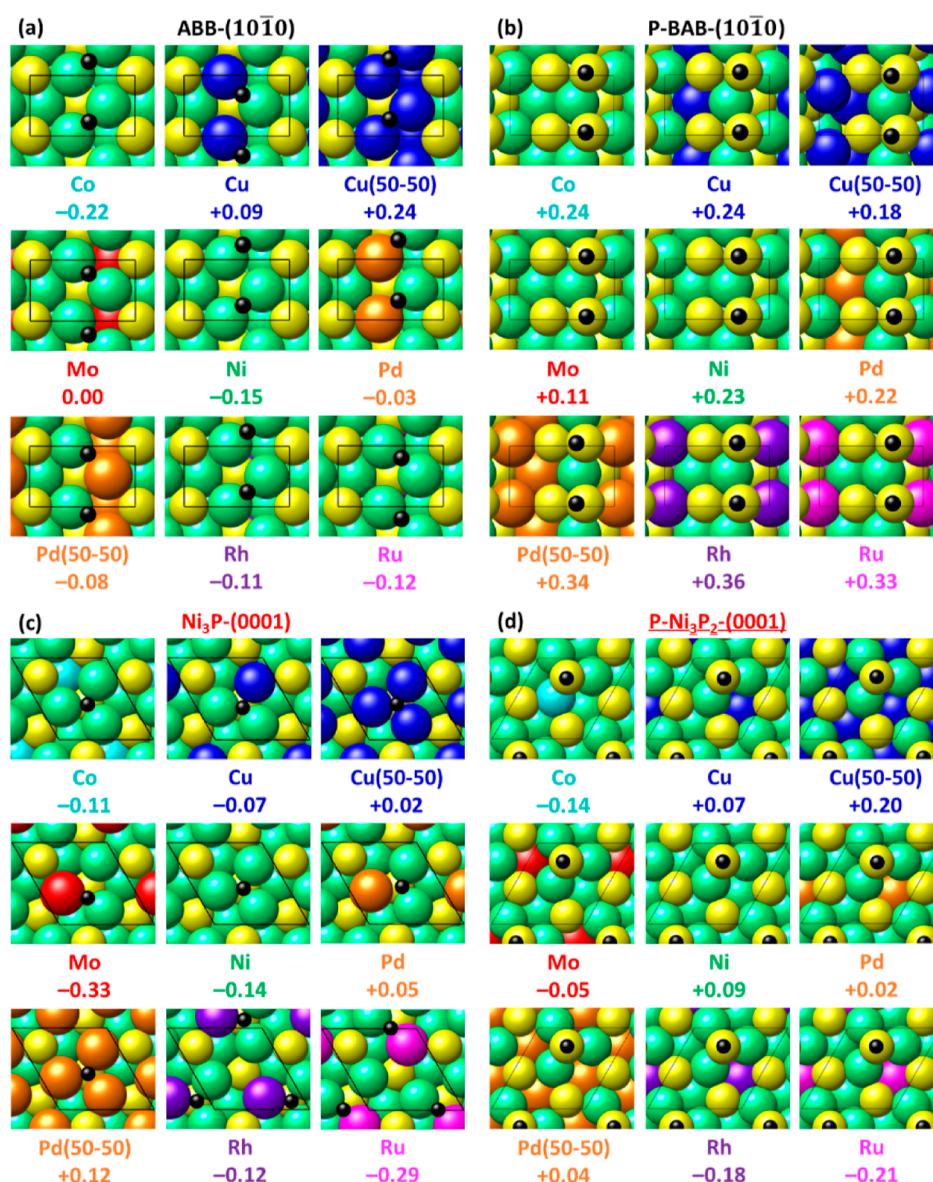
Figure 5. Top views of the optimal H adsorption structure for the (a) ABB- and (b) P-BAB-terminated $Ni_{1.67}M_{0.33}P(10\bar{1}0)$ and (c) Ni_3P- and (d) P-Ni_3P_2-terminated $Ni_{1.67}M_{0.33}P(0001)$ surfaces (M = Co, Cu, Mo, Ni, Pd, Rh, or Ru). Also shown are the H adsorption structures for the Cu- and Pd-enriched $Ni_{1.33}M_{0.67}P$ surfaces with a 1:1 Ni/Cu and Ni/Pd surface-layer composition [Cu(50-50) and Pd(50-50), respectively; see main text for more details]. Calculated adsorption free energies of atomic H (G_H, in eV) are provided below each snapshot. Black lines denote the surface unit cell. Atom colors: black, H; yellow, P; green, Ni; cyan, Co; blue, Cu; red, Mo; orange, Pd; purple, Rh; and pink, Ru.

on a mass-normalized basis. The observed activity trends for $Ni_{2-x}M_xP$ NPs reveal some notable differences from expectations. For example, while Kibsgaard *et al.* found experimentally that MoP and CoP NPs were substantially more active than Ni_2P NPs, the $Ni_{1.54}Mo_{0.46}P$ and $Ni_{1.61}Co_{0.39}P$ NPs in our study appear to be similar to or less active than Ni_2P NPs.[24] The activity for $Ni_{2-x}M_xP$ follows expectations from the study by Zheng *et al.* for the corresponding metal surfaces for Rh, Pd, Co, and Mo but does not agree for Cu;[79] instead of having a negligible effect on the Ni_2P overpotential as the metal performance might suggest, Cu doping substantially increases the overpotential in our case. In other relevant studies, doping Cu into CoP nanowires (under alkaline conditions)[80] and nanosheets (in buffered phosphate)[81] reduced the HER overpotential. The contrasting increase we observed in the overpotential for $Ni_{1.69}Cu_{0.31}P/C$ may indicate

a more subtle relationship between dopant and parent structures than is captured by simple analogy to pure phosphide materials and metals.[21−26] Finally, in a study of a $Ni_{2-x}Co_xP$ series, Liu *et al.* found that activity improved steadily upon doping Co into Ni_2P NPs and upon doping Ni into Co_2P NPs, reaching a maximum near $x = 1$;[23] on this basis, an improvement of up to 10−15 mV in overpotential might be expected for our $Ni_{1.61}Co_{0.39}P$ NPs relative to Ni_2P. Our observation instead of similar or slightly worse activity for $Ni_{1.61}Co_{0.39}P$ may be attributable to differences in NP preparation methods. Figures 4b and S20 show the corresponding Tafel plots for $Ni_{2-x}M_xP$ NPs, Ni_2P NPs, and Pt/C, and the Tafel slopes are summarized in Table 2. The estimated exchange current densities are also provided in Table 2, and no clear trend was observed. Generally, lower Tafel slopes indicate more favorable electrochemical kinetics, and

$Ni_{1.66}Rh_{0.34}P$, the most active TMP material investigated here, exhibited the lowest Tafel slope (58.5 ± 0.4 mV/decade) across the $Ni_{2-x}M_xP$ series. It is noteworthy that the two materials in which surface enrichment was observed for the second metal, $Ni_{1.61}Cu_{0.39}P$ and $Ni_{1.69}Pd_{0.31}P$, exhibited higher Tafel slopes of 101 ± 8 and 96 ± 9 mV/decade, whereas the other phosphide materials had lower slopes in the range of 58.5−70 mV/decade. This electrochemical study thereby established composition-dependent activity trends within an isostructural series that we next sought to explain through computations.

To better understand the influence of the various second metals on the experimental HER activity, DFT calculations were performed to compare G_H on $Ni_{1.67}M_{0.33}P$ surfaces, as G_H is a well-established descriptor for HER activity.[82] Two terminations for both the $(10\bar{1}0)$ and the (0001) Ni_2P surfaces were considered in this analysis (see Computational Methods; each ternary TMP surface is shown in Figure S3), representing the thermodynamic equilibrium surface composition under a range of μ_P. The (0001) surface is most commonly studied[23,24,65−67] due to its lower surface energy relative to other low-index Ni_2P facets,[64] while more corrugated surfaces such as the $(10\bar{1}0)$ surface are also likely exposed and have been identified by Hansen and co-workers to play a key role in HER activity.[83] Furthermore, by assessing the relative ability of the flat (0001) and the corrugated $(10\bar{1}0)$ surfaces to describe the experimental HER activity, insights regarding the facet-dependent catalytic properties of these materials can be obtained. Due to the higher surface concentration of Cu and Pd observed by EDS mapping (Figures S5e−h and 3e−h), $Ni_{1.33}M_{0.67}P$ surfaces with a 50:50 ratio of Ni/Cu and Ni/Pd in the surface layers were also considered alongside the $Ni_{1.67}M_{0.33}P$ analogues (see Figure S3). The minimum-energy adsorption structures and corresponding G_H values for atomic H on each surface are shown in Figure 5. E_B values for the studied high-symmetry adsorption sites on each surface are given in Tables S12−S15. H preferentially binds to threefold metal (M_3) hollow sites or twofold bridge (M_2) sites on the Ni_3P-(0001) surface and to M_2 sites on the ABB-$(10\bar{1}0)$ surface. In contrast, on the P-enriched surfaces where the M_3 and M_2 sites are blocked by surface P adatoms, H preferentially binds to the P adatoms. H adsorption is generally weaker on the P-enriched surfaces, though there are some notable exceptions on the (0001) surfaces. These general trends in the H binding site and strength are consistent with previous reports for Ni_2P.[65,67]

To compare the DFT-calculated G_H values with the experimental HER measurements, η is plotted against G_H for the ABB-$(10\bar{1}0)$, P-BAB-$(10\bar{1}0)$, Ni_3P-(0001), and P-Ni_3P_2-(0001) surfaces. For the P-BAB$(10\bar{1}0)$ surface and the two (0001) surface terminations, the calculated G_H values did not present a clear trend with the experimental HER activity data (Figure S24). However, a clear volcano-shaped trend was observed for the ABB-$(10\bar{1}0)$ surface termination (Figure 6), indicating a good representation of the active site for the HER on $Ni_{1.67}M_{0.33}P$. There are similarities between this volcano plot and the volcano plot for the HER on the bare metals, but there are also noteworthy differences, including that Mo lies on the opposite side of the volcano peak (i.e., binds H too weakly) in the $Ni_{1.6}M_{0.4}P$ system.[79] These differences illustrate the interplay between strain, electronic, and ensemble effects in the $Ni_{1.6}M_{0.4}P$ materials. Bulk-terminated $(10\bar{1}0)$ surfaces are more corrugated and exhibit different preferred adsorption config-
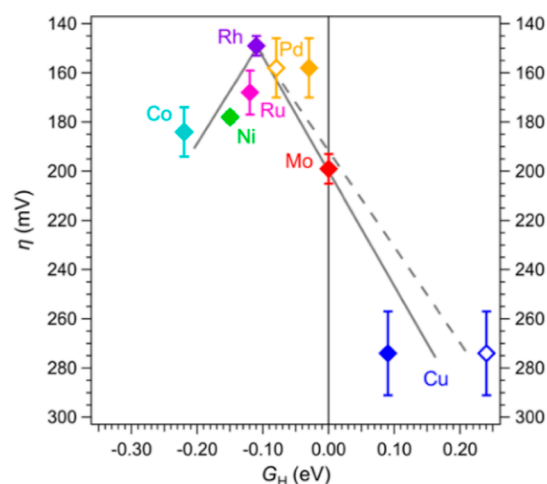

Figure 6. Overpotential (η) *vs* the adsorption free energy of atomic H (G_H) on the ABB-terminated $Ni_{1.67}M_{0.33}P(10\bar{1}0)$ (solid markers) and Cu- and Pd-enriched $Ni_{1.33}M_{0.67}P(10\bar{1}0)$ (open markers) surfaces. Gray lines show the volcano-shaped dependence of η on G_H for the $Ni_{1.67}M_{0.33}P(10\bar{1}0)$ surfaces (solid) and when Cu- and Pd-enriched surfaces are included (dashed).

urations than bulk-terminated (0001) surfaces. For example, H preferentially adsorbs to M_2 sites on the ABB-$(10\bar{1}0)$ surface, compared to M_3 hollow sites on the Ni_3P-terminated (0001) surface; thus, surfaces on which H preferentially adsorbs to corrugated M_2 bridge sites may provide better HER active-site models for the HER on Ni_2P-based ternary metal phosphide materials. Furthermore, the volcano-shaped trend helps explain the enhanced HER activity following the addition of precious metals (Pd, Rh, and Ru) as the hydrogen adsorption energy is modulated more effectively (i.e., slight weakening of H adsorption) with these metals as opposed to the Co-, Cu-, or Mo-modified materials. It should be noted that other low-index facets or the edge sites of $Ni_{2-x}M_xP$ NPs may also provide active sites for the HER[64,83] and that these results indicate that multiple surface facets should be considered for these complex multicomponent materials to determine facet dependence in describing experimental properties trends.

Moreover, to better represent the experimentally observed surface enrichment of the Cu- and Pd-alloyed Ni_2P NPs based on the corresponding EDS elemental maps (Figures S5e−h and 3e−h), additional DFT models of the Cu- and Pd-containing (0001) and $(10\bar{1}0)$ surfaces were constructed such that the surfaces of these materials were enriched to a 50−50 Ni−M composition. The calculated G_H values for the surface-enriched ABB-$(10\bar{1}0)$ surfaces were destabilized by 0.15 eV for the Cu-alloyed surface and stabilized by 0.05 eV for the Pd-alloyed surface. The 50-50 Ni−M surface compositions resulted in a decrease in slope for the right-hand side of the volcano plot (Figure 6, dashed line) which gave a better overall fit to the measured electrocatalytic HER activity compared to the fit obtained with only the non-surface-enriched analogues (linear-fit R^2 of 0.99 *vs* 0.88, respectively). Bader charge analyses and d-band center calculations were performed to elucidate the effect of electronic structure changes in the M-alloyed ABB-$(10\bar{1}0)$ surfaces on the corresponding G_H value (Figure S25). However, neither analysis provided a strong correlation with the G_H values, indicating that the effect of the alloyed metal on G_H is very likely multifactorial with respect to

electronic structure, lattice strain, and M surface *versus* subsurface substitution effects.

Finally, to provide an initial glimpse into the possible evolution of the $Ni_{2-x}M_xP$ NP materials under HER conditions, we compared the properties of pristine and post-HER electrodes for one of the materials, 3.7 wt % $Ni_{1.58}Rh_{0.42}P/C$ (note that because we used a different catalyst batch for this experiment, the composition is slightly different from that used in the other experiments). Because the HER measurements we reported above, designed to determine activity with minimal errors, used a small RDE and a correspondingly small quantity of deposited NPs (0.2 cm^2 electrode × *ca.* 0.025 mg NPs/cm^2 = *ca.* 5 μg NPs per electrode), those electrodes were not conducive to post-reaction characterization. As a result, we devised an alternative electrode preparation method that would preserve the HER treatment conditions while making possible the characterization of coated electrode materials *via* standard techniques. The preparation method is similar to the work we have published previously.[12] Briefly, we hand-painted a catalyst ink containing 3.7 wt % $Ni_{1.58}Rh_{0.42}P/C$ and Nafion onto a large sheet of carbon paper at weight loadings similar to those for the RDE measurements (*ca.* 0.045 mg NPs/cm^2 as determined by ICP-OES; see Table S11). The total surface area was *ca.* 30 cm^2, which was divided into two 15 cm^2 pieces (*ca.* 0.7 mg of NPs per electrode, over 2 orders of magnitude more than on the RDEs). One of the pieces was then tested under HER conditions similar to those already described. The pristine and post-HER electrode pieces were compared using powder XRD, ICP-OES, and STEM. In the powder XRD pattern, the major $Ni_{1.58}Rh_{0.42}P$ peak was preserved without apparent peak shifting or introduction of new peaks (Figure S21). However, ICP-OES and STEM revealed changes in the loaded NPs that indicate some evolution under HER conditions. First, there was an ICP-determined reduction in the loading of Ni (from 0.241 wt % in the pristine electrode to 0.113 wt % in the post-HER electrode), Rh (from 0.0949 to 0.0745%), and P (from 0.083 to 0.071%; Table S11). While both physical delamination and chemical leaching are potential explanations for the reduced loading, the significantly higher reduction in Ni compared to the other elements is more consistent with chemical leaching, for which the 0.5 M H_2SO_4 solution would be expected to dissolve Ni at a higher rate than that for Rh.[17,35] Furthermore, the HAADF-STEM images of the post-HER electrode revealed a change in morphology from spherical to less well-defined (Figure S22). The STEM–EDS mapping shows that the colocation of Ni, Rh, and P was preserved in post-HER samples, with possible loss of some Ni from the surface that would be consistent with the ICP-OES results (Figure S23). We suggest that future studies that aim to improve the electrochemical performance and durability, which was not the focus of this work, could use unsupported $Ni_{2-x}M_xP$ NPs to further investigate the *operando* evolution of ternary phosphide materials.

CONCLUSIONS

A rational solution synthesis method to access ternary $Ni_{2-x}M_xP$ NP compositions was developed using combinations of commercially available or easily prepared metal−phosphine precursors. The particle morphology and crystal phase of the parent Ni_2P NPs were retained across the series. This approach allowed us to directly compare the impact of the second metal on electrocatalytic activity without convoluting factors arising from differences in the NP morphology or phase. The NPs exhibited composition-dependent HER activity, spanning a 125 mV range in overpotential, attributed to the introduction of a second metal into the parent Ni_2P NPs. Computational analysis identified a volcano-shaped trend when the overpotential was plotted against G_H for the stoichiometric ABB-$(10\bar{1}0)$ surfaces, suggesting that the HER over $Ni_{2-x}M_xP$ NPs is facet-dependent and likely requires the presence of corrugated surface features. The ability to independently tune the composition of the ternary nickel phosphide NPs without modifying other key features was crucial to identifying the composition-dependent electrocatalytic activity and the correlation with the $(10\bar{1}0)$ surface. Furthermore, the versatility of the synthetic methodology allows for the preparation of a wide range of compositionally diverse TMP NPs, more broadly enabling the investigation of critical composition−performance relationships for energy applications.

■ ASSOCIATED CONTENT

Ⓢ Supporting Information

The Supporting Information is available free of charge at https://pubs.acs.org/doi/10.1021/acs.chemmater.2c00085.

> TGA profiles; atomic radii and XRD shifts; computational methods; electron microscopy, powder XRD, electrocatalytic HER, and post-HER catalyst characterizations; and computed surfaces and adsorption energies (PDF)

■ AUTHOR INFORMATION

Corresponding Authors

Joshua A. Schaidle − *Catalytic Carbon Transformation and Scale-Up Center, National Renewable Energy Laboratory, Golden, Colorado 80401, United States;* ⓞ orcid.org/0000-0003-2189-5678; Email: joshua.schaidle@nrel.gov

Susan E. Habas − *Catalytic Carbon Transformation and Scale-Up Center, National Renewable Energy Laboratory, Golden, Colorado 80401, United States;* ⓞ orcid.org/0000-0002-3893-8454; Email: susan.habas@nrel.gov

Authors

Courtney A. Downes − *Catalytic Carbon Transformation and Scale-Up Center, National Renewable Energy Laboratory, Golden, Colorado 80401, United States;* ⓞ orcid.org/0000-0001-8631-1579

Kurt M. Van Allsburg − *Catalytic Carbon Transformation and Scale-Up Center, National Renewable Energy Laboratory, Golden, Colorado 80401, United States;* ⓞ orcid.org/0000-0003-4553-6709

Sean A. Tacey − *Catalytic Carbon Transformation and Scale-Up Center, National Renewable Energy Laboratory, Golden, Colorado 80401, United States;* ⓞ orcid.org/0000-0001-7833-6901

Kinga A. Unocic − *Center for Nanophase Materials Sciences, Oak Ridge National Laboratory, Oak Ridge, Tennessee 37831, United States*

Frederick G. Baddour − *Catalytic Carbon Transformation and Scale-Up Center, National Renewable Energy Laboratory, Golden, Colorado 80401, United States;* ⓞ orcid.org/0000-0002-5837-5804

Daniel A. Ruddy − *Catalytic Carbon Transformation and Scale-Up Center, National Renewable Energy Laboratory,*

Golden, Colorado 80401, United States; ⓘ orcid.org/0000-0003-2654-3778

Nicole J. LiBretto − Catalytic Carbon Transformation and Scale-Up Center, National Renewable Energy Laboratory, Golden, Colorado 80401, United States

Max M. O'Connor − Catalytic Carbon Transformation and Scale-Up Center, National Renewable Energy Laboratory, Golden, Colorado 80401, United States; Present Address: Chemistry and Nanoscience Center, National Renewable Energy Laboratory, Golden, CO 80401, USA. Department of Chemistry, University of Colorado, Boulder, CO 80309, USA; ⓘ orcid.org/0000-0001-5446-0799

Carrie A. Farberow − Catalytic Carbon Transformation and Scale-Up Center, National Renewable Energy Laboratory, Golden, Colorado 80401, United States

Complete contact information is available at:
https://pubs.acs.org/10.1021/acs.chemmater.2c00085

Author Contributions

§C.A.D. and K.M.V.A. contributed equally to this work.

Notes

The authors declare no competing financial interest.

REFERENCES

(1) Carenco, S.; Portehault, D.; Boissière, C.; Mézailles, N.; Sanchez, C. Nanoscaled Metal Borides and Phosphides: Recent Developments and Perspectives. *Chem. Rev.* **2013**, *113*, 7981−8065.

(2) Kolny-Olesiak, J. Recent Advances in the Colloidal Synthesis of Ternary Transition Metal Phosphides. *Z. Naturforsch., A: Phys. Sci.* **2019**, *74*, 709−719.

(3) Prins, R.; Bussell, M. E. Metal Phosphides: Preparation, Characterization and Catalytic Reactivity. *Catal. Lett.* **2012**, *142*, 1413−1436.

(4) Joo, J.; Kim, T.; Lee, J.; Choi, S. I.; Lee, K. Morphology-Controlled Metal Sulfides and Phosphides for Electrochemical Water Splitting. *Adv. Mater.* **2019**, *31*, No. e1806682.

(5) Li, Y.; Dong, Z.; Jiao, L. Multifunctional Transition Metal-Based Phosphides in Energy-Related Electrocatalysis. *Adv. Energy Mater.* **2020**, *10*, 1902104.

(6) Pei, Y.; Cheng, Y.; Chen, J.; Smith, W.; Dong, P.; Ajayan, P. M.; Ye, M.; Shen, J. Recent Developments of Transition Metal Phosphides as Catalysts in the Energy Conversion field. *J. Mater. Chem. A* **2018**, *6*, 23220−23243.

(7) Callejas, J. F.; Read, C. G.; Roske, C. W.; Lewis, N. S.; Schaak, R. E. Synthesis, Characterization, and Properties of Metal Phosphide Catalysts for the Hydrogen-Evolution Reaction. *Chem. Mater.* **2016**, *28*, 6017−6044.

(8) Shi, Y.; Zhang, B. Recent Advances in Transition Metal Phosphide Nanomaterials: Synthesis and Applications in Hydrogen Evolution Reaction. *Chem. Soc. Rev.* **2016**, *45*, 1529−1541.

(9) Calvinho, K. U. D.; Laursen, A. B.; Yap, K. M. K.; Goetjen, T. A.; Hwang, S.; Murali, N.; Mejia-Sosa, B.; Lubarski, A.; Teeluck, K. M.; Hall, E. S.; Garfunkel, E.; Greenblatt, M.; Dismukes, G. C. Selective CO_2 Reduction to C_3 and C_4 Oxyhydrocarbons on Nickel Phosphides at Overpotentials as Low as 10 mV. *Energy Environ. Sci.* **2018**, *11*, 2550−2559.

(10) Li, H.; Wen, P.; Itanze, D. S.; Hood, Z. D.; Ma, X.; Kim, M.; Adhikari, S.; Lu, C.; Dun, C.; Chi, M.; Qiu, Y.; Geyer, S. M. Colloidal Silver Diphosphide (AgP_2) Nanocrystals as Low Overpotential Catalysts for CO_2 Reduction to Tunable Syngas. *Nat. Commun.* **2019**, *10*, 5724.

(11) Ji, L.; Li, L.; Ji, X.; Zhang, Y.; Mou, S.; Wu, T.; Liu, Q.; Li, B.; Zhu, X.; Luo, Y.; Shi, X.; Asiri, A. M.; Sun, X. Highly Selective Electrochemical Reduction of to Alcohols on an FeP Nanoarray. *Angew. Chem., Int. Ed.* **2020**, *59*, 758−762.

(12) Downes, C. A.; Libretto, N. J.; Harman-Ware, A. E.; Happs, R. M.; Ruddy, D. A.; Baddour, F. G.; Ferrell, J. R., III; Habas, S. E.; Schaidle, J. A. Electrocatalytic CO_2 Reduction over Cu_3P Nanoparticles Generated Via a Molecular Precursor Route. *ACS Appl. Energy Mater.* **2020**, *3*, 10435−10446.

(13) Laursen, A. B.; Calvinho, K. U. D.; Goetjen, T. A.; Yap, K. M. K.; Hwang, S.; Yang, H.; Garfunkel, E.; Dismukes, G. C. CO_2 Electro-Reduction on Cu_3P: Role of Cu(I) Oxidation State and Surface Facet Structure in C1-Formate Production and H_2 Selectivity. *Electrochim. Acta* **2021**, *391*, 138889.

(14) Calvinho, K. U. D.; Alherz, A. W.; Yap, K. M. K.; Laursen, A. B.; Hwang, S.; Bare, Z. J. L.; Clifford, Z.; Musgrave, C. B.; Dismukes, G. C. Surface Hydrides on Fe_2P Electrocatalyst Reduce at Low Overpotential: Steering Selectivity to Ethylene Glycol. *J. Am. Chem. Soc.* **2021**, *143*, 21275.

(15) Kucernak, A. R. J.; Sundaram, V. N. N. Nickel Phosphide: The Effect of Phosphorus Content on Hydrogen Evolution Activity and Corrosion Resistance in Acidic Medium. *J. Mater. Chem. A* **2014**, *2*, 17435−17445.

(16) Pan, Y.; Liu, Y.; Zhao, J.; Yang, K.; Liang, J.; Liu, D.; Hu, W.; Liu, D.; Liu, Y.; Liu, C. Monodispersed Nickel Phosphide Nanocrystals with Different Phases: Synthesis, Characterization and Electrocatalytic Properties for Hydrogen Evolution. *J. Mater. Chem. A* **2015**, *3*, 1656−1665.

(17) Laursen, A. B.; Patraju, K. R.; Whitaker, M. J.; Retuerto, M.; Sarkar, T.; Yao, N.; Ramanujachary, K. V.; Greenblatt, M.; Dismukes, G. C. Nanocrystalline Ni_5P_4: A Hydrogen Evolution Electrocatalyst of

Exceptional Efficiency in Both Alkaline and Acidic Media. *Energy Environ. Sci.* **2015**, *8*, 1027−1034.

(18) Callejas, J. F.; Read, C. G.; Popczun, E. J.; McEnaney, J. M.; Schaak, R. E. Nanostructured Co$_2$P Electrocatalyst for the Hydrogen Evolution Reaction and Direct Comparison with Morphologically Equivalent CoP. *Chem. Mater.* **2015**, *27*, 3769−3774.

(19) Pan, Y.; Lin, Y.; Chen, Y.; Liu, Y.; Liu, C. Cobalt Phosphide-Based Electrocatalysts: Synthesis and Phase Catalytic Activity Comparison for Hydrogen Evolution. *J. Mater. Chem. A* **2016**, *4*, 4745−4754.

(20) Seo, B.; Baek, D. S.; Sa, Y. J.; Joo, S. H. Shape Effects of Nickel Phosphide Nanocrystals on Hydrogen Evolution Reaction. *CrystEngComm* **2016**, *18*, 6083−6089.

(21) Mutinda, S. I.; Li, D.; Kay, J.; Brock, S. L. Synthesis and Characterization of Co$_{2-x}$Rh$_x$P Nanoparticles and Their Catalytic Activity Towards the Oxygen Evolution Reaction. *J. Mater. Chem. A* **2018**, *6*, 12142−12152.

(22) Liyanage, D. R.; Li, D.; Cheek, Q. B.; Baydoun, H.; Brock, S. L. Synthesis and Oxygen Evolution Reaction (OER) Catalytic Performance of Ni$_{2-x}$Ru$_x$P Nanocrystals: Enhancing Activity by Dilution of the Noble Metal. *J. Mater. Chem. A* **2017**, *5*, 17609−17618.

(23) Liu, J.; Wang, Z.; David, J.; Llorca, J.; Li, J.; Yu, X.; Shavel, A.; Arbiol, J.; Meyns, M.; Cabot, A. Colloidal Ni$_{2-x}$Co$_x$P Nanocrystals for the Hydrogen Evolution Reaction. *J. Mater. Chem. A* **2018**, *6*, 11453−11462.

(24) Kibsgaard, J.; Tsai, C.; Chan, K.; Benck, J. D.; Nørskov, J. K.; Abild-Pedersen, F.; Jaramillo, T. F. Designing an Improved Transition Metal Phosphide Catalyst for Hydrogen Evolution Using Experimental and Theoretical Trends. *Energy Environ. Sci.* **2015**, *8*, 3022−3029.

(25) Tang, C.; Gan, L.; Zhang, R.; Lu, W.; Jiang, X.; Asiri, A. M.; Sun, X.; Wang, J.; Chen, L. Ternary Fe$_x$Co$_{1-x}$P Nanowire Array as a Robust Hydrogen Evolution Reaction Electrocatalyst with Pt-Like Activity: Experimental and Theoretical Insight. *Nano Lett.* **2016**, *16*, 6617−6621.

(26) Tan, Y.; Wang, H.; Liu, P.; Shen, Y.; Cheng, C.; Hirata, A.; Fujita, T.; Tang, Z.; Chen, M. Versatile Nanoporous Bimetallic Phosphides Towards Electrochemical Water Splitting. *Energy Environ. Sci.* **2016**, *9*, 2257−2261.

(27) Brock, S. L.; Perera, S. C.; Stamm, K. L. Chemical Routes for Production of Transition-Metal Phosphides on the Nanoscale: Implications for Advanced Magnetic and Catalytic Materials. *Chem.—Eur. J.* **2004**, *10*, 3364−3371.

(28) Henkes, A. E.; Vasquez, Y.; Schaak, R. E. Converting Metals into Phosphides: A General Strategy for the Synthesis of Metal Phosphide Nanocrystals. *J. Am. Chem. Soc.* **2007**, *129*, 1896−1897.

(29) Carenco, S.; Hu, Y.; Florea, I.; Ersen, O.; Boissière, C.; Mézailles, N.; Sanchez, C. Metal-Dependent Interplay between Crystallization and Phosphorus Diffusion During the Synthesis of Metal Phosphide Nanoparticles. *Chem. Mater.* **2012**, *24*, 4134−4145.

(30) Mundy, M. E.; Ung, D.; Lai, N. L.; Jahrman, E. P.; Seidler, G. T.; Cossairt, B. M. Aminophosphines as Versatile Precursors for the Synthesis of Metal Phosphide Nanocrystals. *Chem. Mater.* **2018**, *30*, 5373−5379.

(31) Tappan, B. A.; Chen, K.; Lu, H.; Sharada, S. M.; Brutchey, R. L. Synthesis and Electrocatalytic HER Studies of Carbene-Ligated Cu$_{3-x}$P Nanocrystals. *ACS Appl. Mater. Interfaces* **2020**, *12*, 16394−16401.

(32) Sun, M.; Liu, H.; Qu, J.; Li, J. Earth-Rich Transition Metal Phosphide for Energy Conversion and Storage. *Adv. Energy Mater.* **2016**, *6*, 1600087.

(33) Li, S.-H.; Qi, M.-Y.; Tang, Z.-R.; Xu, Y.-J. Nanostructured Metal Phosphides: From Controllable Synthesis to Sustainable Catalysis. *Chem. Soc. Rev.* **2021**, *50*, 7539−7586.

(34) Habas, S. E.; Baddour, F. G.; Ruddy, D. A.; Nash, C. P.; Wang, J.; Pan, M.; Hensley, J. E.; Schaidle, J. A. A Facile Molecular Precursor Route to Metal Phosphide Nanoparticles and Their Evaluation as Hydrodeoxygenation Catalysts. *Chem. Mater.* **2015**, *27*, 7580−7592.

(35) Mutinda, S. I.; Batugedara, T. N.; Brown, B.; Adeniran, O.; Liu, Z.-F.; Brock, S. L. Rh$_2$P Activity at a Fraction of the Cost? Co$_{2-x}$Rh$_x$P Nanoparticles as Electrocatalysts for the Hydrogen Evolution Reaction in Acidic Media. *ACS Appl. Energy Mater.* **2021**, *4*, 946−955.

(36) Yoon, K. Y.; Jang, Y.; Park, J.; Hwang, Y.; Koo, B.; Park, J.-G.; Hyeon, T. Synthesis of Uniform-Sized Bimetallic Iron−Nickel Phosphide Nanorods. *J. Solid State Chem.* **2008**, *181*, 1609−1613.

(37) Hitihami-Mudiyanselage, A.; Arachchige, M. P.; Seda, T.; Lawes, G.; Brock, S. L. Synthesis and Characterization of Discrete Fe$_x$Ni$_{2-x}$P Nanocrystals (0 < x < 2): Compositional Effects on Magnetic Properties. *Chem. Mater.* **2015**, *27*, 6592−6600.

(38) Liyanage, D. R.; Danforth, S. J.; Liu, Y.; Bussell, M. E.; Brock, S. L. Simultaneous Control of Composition, Size, and Morphology in Discrete Ni$_{2-x}$Co$_x$P Nanoparticles. *Chem. Mater.* **2015**, *27*, 4349−4357.

(39) Danforth, S. J.; Liyanage, D. R.; Hitihami-Mudiyanselage, A.; Ilic, B.; Brock, S. L.; Bussell, M. E. Probing Hydrodesulfurization over Bimetallic Phosphides Using Monodisperse Ni$_{2-x}$M$_x$P Nanoparticles Encapsulated in Mesoporous Silica. *Surf. Sci.* **2016**, *648*, 126−135.

(40) Hegedus, L. S.; Perry, R. J. Phosphinecarbonylnitrosylacylcobaltate Complexes as Acyl Transfer Reagents. Acylation of Allylic Halides, Conjugated Enones, and Quinones. *J. Org. Chem.* **1985**, *50*, 4955−4960.

(41) Schneider, C. A.; Rasband, W. S.; Eliceiri, K. W. NIH Image to ImageJ: 25 Years of Image Analysis. *Nat. Methods* **2012**, *9*, 671.

(42) Popczun, E. J.; McKone, J. R.; Read, C. G.; Biacchi, A. J.; Wiltrout, A. M.; Lewis, N. S.; Schaak, R. E. Nanostructured Nickel Phosphide as an Electrocatalyst for the Hydrogen Evolution Reaction. *J. Am. Chem. Soc.* **2013**, *135*, 9267−9270.

(43) Alcaide, F.; Álvarez, G.; Cabot, P. L.; Genova-Koleva, R.; Grande, H.-J.; Miguel, O. Effect of the Solvent in the Catalyst Ink Preparation on the Properties and Performance of Unsupported PtRu Catalyst Layers in Direct Methanol Fuel Cells. *Electrochim. Acta* **2017**, *231*, 529−538.

(44) Huang, D.-C.; Yu, P.-J.; Liu, F.-J.; Huang, S.-L.; Hsueh, K.-L.; Chen, Y.-C.; Wu, C.-H.; Chang, W.-C.; Tsau, F.-H. Effect of Dispersion Solvent in Catalyst Ink on Proton Exchange Membrane Fuel Cell Performance. *Int. J. Electrochem. Sci.* **2011**, *6*, 2551−2565.

(45) Ngo, T. T.; Yu, T. L.; Lin, H.-L. Influence of the Composition of Isopropyl Alcohol/Water Mixture Solvents in Catalyst Ink Solutions on Proton Exchange Membrane Fuel Cell Performance. *J. Power Sources* **2013**, *225*, 293−303.

(46) Ngo, T. T.; Yu, T. L.; Lin, H.-L. Nafion-Based Membrane Electrode Assemblies Prepared from Catalyst Inks Containing Alcohol/Water Solvent Mixtures. *J. Power Sources* **2013**, *238*, 1−10.

(47) Shimanuki, J.; Takahashi, S.; Tohma, H.; Ohma, A.; Ishihara, A.; Ito, Y.; Nishino, Y.; Miyazawa, A. Microstructural Observation of Fuel Cell Catalyst Inks by Cryo-SEM and Cryo-TEM. *Microscopy* **2017**, *66*, 204−208.

(48) Shukla, S.; Bhattacharjee, S.; Secanell, M. Rationalizing Catalyst Inks for PEMFC Electrodes Based on Colloidal Interactions. *ECS Trans.* **2013**, *58*, 1409−1428.

(49) Therdthianwong, A.; Ekdharmasuit, P.; Therdthianwong, S. Fabrication and Performance of Membrane Electrode Assembly Prepared by a Catalyst-Coated Membrane Method: Effect of Solvents Used in a Catalyst Ink Mixture. *Energy Fuels* **2010**, *24*, 1191−1196.

(50) Wuttikid, K.; Worayos, N.; Punyawudho, K. Analysis of Catalyst Ink Compositions for Fabricating Membrane Electrode Assemblies in PEM Fuel Cells. *Chiang Mai Univ. J. Nat. Sci.* **2017**, *16*, 275−281.

(51) Inaba, M.; Quinson, J.; Arenz, M. Ph Matters: The Influence of the Catalyst Ink on the Oxygen Reduction Activity Determined in Thin Film Rotating Disk Electrode Measurements. *J. Power Sources* **2017**, *353*, 19−27.

(52) Jung, C.-Y.; Kim, W.-J.; Yi, S.-C. Optimization of Catalyst Ink Composition for the Preparation of a Membrane Electrode Assembly in a Proton Exchange Membrane Fuel Cell Using the Decal Transfer. *Int. J. Hydrogen Energy* **2012**, *37*, 18446−18454.

(53) Shinozaki, K.; Zack, J. W.; Pylypenko, S.; Pivovar, B. S.; Kocha, S. S. Oxygen Reduction Reaction Measurements on Platinum Electrocatalysts Utilizing Rotating Disk Electrode Technique. *J. Electrochem. Soc.* **2015**, *162*, F1384−F1396.

(54) Pollet, B. G.; Goh, J. T. E. The Importance of Ultrasonic Parameters in the Preparation of Fuel Cell Catalyst Inks. *Electrochim. Acta* **2014**, *128*, 292−303.

(55) Jung, S.; McCrory, C. C. L.; Ferrer, I. M.; Peters, J. C.; Jaramillo, T. F. Benchmarking Nanoparticulate Metal Oxide Electrocatalysts for the Alkaline Water Oxidation Reaction. *J. Mater. Chem. A* **2016**, *4*, 3068−3076.

(56) Reier, T.; Oezaslan, M.; Strasser, P. Electrocatalytic Oxygen Evolution Reaction (OER) on Ru, Ir, and Pt Catalysts: A Comparative Study of Nanoparticles and Bulk Materials. *ACS Catal.* **2012**, *2*, 1765−1772.

(57) Gong, M.; Li, Y.; Wang, H.; Liang, Y.; Wu, J. Z.; Zhou, J.; Wang, J.; Regier, T.; Wei, F.; Dai, H. An Advanced Ni-Fe Layered Double Hydroxide Electrocatalyst for Water Oxidation. *J. Am. Chem. Soc.* **2013**, *135*, 8452−8455.

(58) Kresse, G.; Furthmüller, J. Efficient Iterative Schemes for Ab Initio Total-Energy Calculations Using a Plane-Wave Basis Set. *Phys. Rev. B: Condens. Matter Mater. Phys.* **1996**, *54*, 11169−11186.

(59) Kresse, G.; Furthmüller, J. Efficiency of Ab-Initio Total Energy Calculations for Metals and Semiconductors Using a Plane-Wave Basis Set. *Comput. Mater. Sci.* **1996**, *6*, 15−50.

(60) Perdew, J. P.; Burke, K.; Ernzerhof, M. Generalized Gradient Approximation Made Simple. *Phys. Rev. Lett.* **1996**, *77*, 3865−3868.

(61) Blöchl, P. E. Projector Augmented-Wave Method. *Phys. Rev. B: Condens. Matter Mater. Phys.* **1994**, *50*, 17953−17979.

(62) Kresse, G.; Joubert, D. From Ultrasoft Pseudoptentials to the Projector Augmented-Wave Method. *Phys. Rev. B: Condens. Matter Mater. Phys.* **1999**, *59*, 1758−1775.

(63) Grimme, S.; Antony, J.; Ehrlich, S.; Krieg, H. A Consistent and Accurate Ab Initio Parametrization of Density Functional Dispersion Correction (DFT-D) for the 94 Elements H-Pu. *J. Chem. Phys.* **2010**, *132*, 154104.

(64) He, J.; Morales-García, Á.; Bludský, O.; Nachtigall, P. The Surface Stability and Equilibrium Crystal Morphology of Ni_2P Nanoparticles and Nanowires from an Ab Initio Atomistic Thermodynamic Approach. *CrystEngComm* **2016**, *18*, 3808−3818.

(65) Wexler, R. B.; Martirez, J. M. P.; Rappe, A. M. Active Role of Phosphorus in the Hydrogen Evolving Activity of Nickel Phosphide (0001) Surfaces. *ACS Catal.* **2017**, *7*, 7718−7725.

(66) Partanen, L.; Hakala, M.; Laasonen, K. Hydrogen Adsorption Trends on Various Metal-Doped Ni_2P Surfaces for Optimal Catalyst Design. *Phys. Chem. Chem. Phys.* **2018**, *21*, 184−191.

(67) Moon, J.-S.; Jang, J.-H.; Kim, E.-G.; Chung, Y.-H.; Yoo, S. J.; Lee, Y.-K. The Nature of Active Sites of Ni_2P Electrocatalyst for Hydrogen Evolution Reaction. *J. Catal.* **2015**, *326*, 92−99.

(68) Monkhorst, H. J.; Pack, J. D. Special Points for Brillouin-Zone Integrations. *Phys. Rev. B: Solid State* **1976**, *13*, 5188−5192.

(69) Wang, X.; Wan, F.; Gao, Y.; Liu, J.; Jiang, K. Synthesis of High-Quality Ni_2P Hollow Sphere Via a Template-Free Surfactant-Assisted Solvothermal Route. *J. Cryst. Growth* **2008**, *310*, 2569−2574.

(70) Wexler, R. B.; Martirez, J. M. P.; Rappe, A. M. Stable Phosphorus-Enriched (0001) Surfaces of Nickel Phosphides. *Chem. Mater.* **2016**, *28*, 5365−5372.

(71) Wang, J.; Johnston-Peck, A. C.; Tracy, J. B. Nickel Phosphide Nanoparticles with Hollow, Solid, and Amorphous Structures. *Chem. Mater.* **2009**, *21*, 4462−4467.

(72) Muthuswamy, E.; Savithra, G. H. L.; Brock, S. L. Synthetic Levers Enabling Independent Control of Phase, Size, and Morphology in Nickel Phosphide Nanoparticles. *ACS Nano* **2011**, *5*, 2402−2411.

(73) Moreau, L. M.; Ha, D.-H.; Zhang, H.; Hovden, R.; Muller, D. A.; Robinson, R. D. Defining Crystalline/Amorphous Phases of Nanoparticles through X-Ray Absorption Spectroscopy and X-Ray Diffraction: The Case of Nickel Phosphide. *Chem. Mater.* **2013**, *25*, 2394−2403.

(74) Ung, D.; Cossairt, B. M. Effect of Surface Ligands on CoP for the Hydrogen Evolution Reaction. *ACS Appl. Energy Mater.* **2019**, *2*, 1642−1645.

(75) Kim, K.-Y.; Habas, S. E.; Schaidle, J. A.; Logan, B. E. Application of Phase-Pure Nickel Phosphide Nanoparticles as Cathode Catalysts for Hydrogen Production in Microbial Electrolysis Cells. *Bioresour. Technol.* **2019**, *293*, 122067.

(76) McCrory, C. C. L.; Jung, S.; Ferrer, I. M.; Chatman, S. M.; Peters, J. C.; Jaramillo, T. F. Benchmarking Hydrogen Evolving Reaction and Oxygen Evolving Reaction Electrocatalysts for Solar Water Splitting Devices. *J. Am. Chem. Soc.* **2015**, *137*, 4347−4357.

(77) Wang, F.; Zhang, Y.; Liu, Z.; Du, Z.; Zhang, L.; Ren, J.; Qu, X. A Biocompatible Heterogeneous MOF-Cu Catalyst for In Vivo Drug Synthesis in Targeted Subcellular Organelles. *Angew. Chem., Int. Ed.* **2019**, *58*, 6987−6992.

(78) Wei, C.; Rao, R. R.; Peng, J.; Huang, B.; Stephens, I. E. L.; Risch, M.; Xu, Z. J.; Shao-Horn, Y. Recommended Practices and Benchmark Activity for Hydrogen and Oxygen Electrocatalysis in Water Splitting and Fuel Cells. *Adv. Mater.* **2019**, *31*, No. e1806296.

(79) Zheng, Y.; Jiao, Y.; Jaroniec, M.; Qiao, S. Z. Advancing the Electrochemistry of the Hydrogen-Evolution Reaction through Combining Experiment and Theory. *Angew. Chem., Int. Ed.* **2015**, *54*, 52−65.

(80) Xu, K.; Sun, Y.; Sun, Y.; Zhang, Y.; Jia, G.; Zhang, Q.; Gu, L.; Li, S.; Li, Y.; Fan, H. J. Yin-Yang Harmony: Metal and Nonmetal Dual-Doping Boosts Electrocatalytic Activity for Alkaline Hydrogen Evolution. *ACS Energy Lett.* **2018**, *3*, 2750−2756.

(81) Yan, L.; Zhang, B.; Zhu, J.; Li, Y.; Tsiakaras, P.; Kang Shen, P. Electronic Modulation of Cobalt Phosphide Nanosheet Arrays Via Copper Doping for Highly Efficient Neutral-pH Overall Water Splitting. *Appl. Catal., B* **2020**, *265*, 118555.

(82) Nørskov, J. K.; Bligaard, T.; Logadottir, A.; Kitchin, J. R.; Chen, J. G.; Pandelov, S.; Stimming, U. Trends in the Exchange Current for Hydrogen Evolution. *J. Electrochem. Soc.* **2005**, *152*, J23.

(83) Hansen, M. H.; Stern, L.-A.; Feng, L.; Rossmeisl, J.; Hu, X. Widely Available Active Sites on Ni_2P for Electrochemical Hydrogen Evolution—Insights from First Principles Calculations. *Phys. Chem. Chem. Phys.* **2015**, *17*, 10823−10829.